PHOTONICS Research

Hybrid-integrated high-performance microwave photonic filter with switchable response

Yuansheng Tao,[1] Haowen Shu,[1] Xingjun Wang,[1,2,3,4,*] Ming Jin,[1] Zihan Tao,[1] Fenghe Yang,[3] Jingbo Shi,[1] and Jun Qin[1]

[1]State Key Laboratory of Advanced Optical Communication Systems and Networks, Department of Electronics, School of Electronics Engineering and Computer Science, Peking University, Beijing 100871, China
[2]Frontier Science Center for Nano-optoelectronics, Peking University, Beijing 100871, China
[3]Peking University Yangtze Delta Institute of Optoelectronics, Nantong 226010, China
[4]Peng Cheng Laboratory, Shenzhen 518055, China
*Corresponding author: xjwang@pku.edu.cn

Received 9 April 2021; revised 11 June 2021; accepted 16 June 2021; posted 16 June 2021 (Doc. ID 427393); published 30 July 2021

The integrated microwave photonic filter (MPF), as a compelling candidate for next-generation radio-frequency (RF) applications, has been widely investigated for decades. However, most integrated MPFs reported thus far have merely incorporated passive photonic components onto a chip-scale platform, while all necessary active devices are still bulk and discrete. Though few attempts to higher photonic integration of MPFs have been executed, the achieved filtering performances are fairly limited, which impedes the pathway to practical deployments. Here, we demonstrate, for the first time to our knowledge, an all-integrated MPF combined with high filtering performances, through hybrid integration of an InP chip-based laser and a monolithic silicon photonic circuit consisting of a dual-drive Mach–Zehnder modulator, a high-Q ring resonator, and a photodetector. This integrated MPF exhibits a high spectral resolution as narrow as 360 MHz, a wide-frequency tunable range covering the S-band to K-band (3 to 25 GHz), and a large rejection ratio of >40 dB. Moreover, the filtering response can be agilely switched between the bandpass and band-stop function with a transient respond time (~48 μs). Compared with previous MPFs in a similar integration level, the obtained spectral resolution in this work is dramatically improved by nearly one order of magnitude, while the valid frequency tunable range is broadened more than twice, which can satisfy the essential filtering requirements in actual RF systems. As a paradigm demonstration oriented to real-world scenarios, high-resolution RF filtering of realistic microwave signals aiming for interference rejection and channel selection is performed. Our work points out a feasible route to a miniaturized, high-performance, and cost-effective MPF leveraging hybrid integration approach, thus enabling a range of RF applications from wireless communication to radar toward the higher-frequency region, more compact size, and lower power consumption.

https://doi.org/10.1364/PRJ.427393

1. INTRODUCTION

Microwave filters are indispensable building blocks in radio frequency (RF) receivers and are paramount to myriad applications, including radar, wireless communication, and sensing [1–3]. Due to the electronic bottleneck, traditional electronic microwave filters are facing significant challenges for meeting the exponentially increasing capacity in next-generation RF systems [4,5]. For instance, 6G wireless networks in the near future are expected to support an ultrahigh data transmission rate of 100 Gb/s in which the higher RF spectrum region such as mm wave (30 to 300 GHz) shall be harnessed [6,7], while the valid operation frequency of existing electronic filters is commonly restricted below 10 GHz [8]. As a promising alternative, microwave photonic filters (MPFs), which perform filtering operations in the optical domain, are capable of offering wideband tunability along with high stability, low latency, and strong immunity to electromagnetic interference [9]. Such outstanding advantages have propelled abundant explorations on MPFs over the past decades [10–14]. Nevertheless, conventional MPFs are implemented based on bulk devices or benchtop instruments and hence are plagued by the limitations in system cost, space, and power consumption.

Recently, the integration of MPF systems onto a chip-scale platform has been driven by advances in nanophotonic fabrication techniques, which is termed "integrated MPFs" [5]. Considerable progress has been made on integrated MPFs that explore different schemes based on microring resonators (MRRs) [15,16], Mach–Zehnder interferometers (MZIs) [17],

waveguide Bragg gratings [18], microcombs [19,20], on-chip stimulated Brillouin scattering [21,22], etc. These demonstrations prove the inherent superiorities of integrated MPFs, in terms of compact footprint, light weight, and scalability. However, in most reported integrated MPFs, only the passive components are incorporated on chip, while all necessary active devices, including lasers, modulators, and photodetectors (PDs), are off-chip and based on fiber connections. The overall systems of such integrated MPFs are still complex, with high power dissipation and sensitivity to environmental fluctuations, thus imposing restrictions on their deployments in real RF systems. Therefore, a higher degree of photonic integration is becoming an urgent pursuit for the implementation of integrated MPFs.

To date, few attempts to create an MPF in high photonic integration have been executed based on monolithic platforms, including indium phosphorus (InP) and silicon platforms. The InP platform can enable monolithic integration of all necessary active and passive devices, on which the first fully integrated MPF was realized [23]. However, issues related to large propagation loss severely limit the accessible spectral resolution on this platform (e.g., 3 dB bandwidth is 2.5 to 5.5 GHz in Ref. [23]). Compared with the InP platform, the silicon photonics platform offers moderately low loss, together with small size, high-volume production, and compatibility with electronic circuits [24]. More recently, MPFs in a high integration level based on a silicon platform have also been demonstrated [25,26]. For example, a silicon highly integrated bandpass MPF consisting of a phase modulator, a micro-disk resonator, and a PD was reported; this MPF features a passband bandwidth of 1.93 GHz, a frequency tunable range within 3 to 10 GHz, and an extinction ratio of 15 dB [25]. Nevertheless, a chip-scale laser source has always been absent for silicon-integrated MPFs due to an indirect bandgap.

Despite these achievements, several pivotal problems still persist, hindering the follow-up development of integrated MPFs. First, the realized filtering performances as indicated above are relatively limited and not competitive with those of discrete MPFs. Generally, toward next-generation RF applications, the integrated MPF is supposed to meet rigorous filtering characteristics, including a sub-GHz bandwidth [4], large rejection ratio (>40 dB [5]), and high frequency band (≥18 GHz [27]). Second, the former MPFs in high photonic integration have only realized a single filtering function. While in the modern frequency-agile RF environment, the reconfigurable microwave filters, especially those with bandpass/band-stop switchable response have gained growing necessity due to potential benefits for improving versatility and reducing volume [28–30], which have not been demonstrated in all-integrated format. Moreover, all integrated MPFs reported until now are implemented based on individual photonic platforms (most are InP, Si or Si_3N_4), since the integration materials have their own strengths and weaknesses, providing all essential components with required characteristics of a complete MPF are fairly challenging on a single platform [31]. Typically, Si and Si_3N_4 platforms are ideal candidates to realize high spectral resolution due to low loss; however, laser integration on these substrates has remained a longstanding difficulty. Fortunately, however, hybrid integration has recently been recognized as a feasible avenue to construct efficient bridges among different material platforms [32], which mainly relies on optical connections in the form of direct facet-to-facet coupling [33], micro-optics [34], or photonic wire bonding [35]. Hybrid integration of multimaterial platforms carried out in transceivers [36,37], quantum photonics [38], frequency synthesizers [39], and so forth, however, remains unexplored for creating a completely integrated MPF.

In this work, we address all the aforementioned points and demonstrate an all-integrated high-performance MPF. This integrated MPF is realized through hybrid integration of an InP chip-scale laser and a monolithic silicon chip consisting of a dual-drive Mach–Zehnder modulator (DDMZM), a high-Q MRR, and a PD. The filtering response of this integrated MPF can be flexibly switched between band-stop and bandpass functions by controlling bias DC voltage of the DDMZM. For the band-stop filtering, a wide-frequency tunable range of 3 to 25 GHz and a narrow 3 dB bandwidth of 380 to 450 MHz were achieved, along with a high rejection ratio of >40 dB. For the bandpass filtering, the frequency tunable range and 3 dB bandwidth were measured as 3 to 21 GHz and 360 to 470 MHz, respectively. In regard to the RF link performances, an RF gain of −28.2 dB, a noise figure of 51.2 dB, and a spurious-free dynamic range (SFDR) of 99.7 $\mathrm{dB \cdot Hz^{2/3}}$ were obtained. Compared with former MPFs in a similar photonic integration degree, the spectral resolution is greatly promoted by nearly one order of magnitude, while the tunable range is extended more than twice. Notably, thanks to such unparalleled filtering performances, high-resolution RF filtering of actual microwave signals is given, which, to our best knowledge, has never been performed by a highly integrated MPF before.

2. PRINCIPLES AND DESIGN

The architecture of the hybrid integrated MPF is illustrated in Fig. 1(a), incorporating an InP waveguide-integrated distributed feedback (DFB) laser and a monolithic silicon chip onto the submount. The silicon chip consists of three key devices: a DDMZM, a high-Q racetrack MRR, and a PD. Figure 1(b) presents the operation principles for the bandpass/band-stop switchable filtering of the integrated MPF. A continuous-wave (CW) light with a center angular frequency of ω_c is generated by the InP laser and then is routed to the DDMZM. The input RF signal with an angular frequency of ω_{rf} is applied to the DDMZM with the aid of a 90° RF hybrid. By adjusting the phase difference φ_{DC} between two MZI arms via a thermal phase shifter, both the equivalent phase modulation (EPM, $\varphi_{\mathrm{DC}} = 0$) and the asymmetric double-sideband modulation (AS-DSB, $0 < \varphi_{\mathrm{DC}} < \pi/2$ or $\pi/2 < \varphi_{\mathrm{DC}} < \pi$) schemes can be acquired. This provides the ability to switch the filtering response between bandpass (based on EPM) and band-stop (based on AS-DSB). Subsequently, the modulated optical spectra are tailored by the resonance notch of the high-Q MRR. Finally, the processed optical spectra are translated to corresponding RF filtering response by means of the PD. A detailed analysis can be found in Appendix A.

The monolithic silicon photonics chip is designed in-house and fabricated on a 220 nm SOI platform leveraging

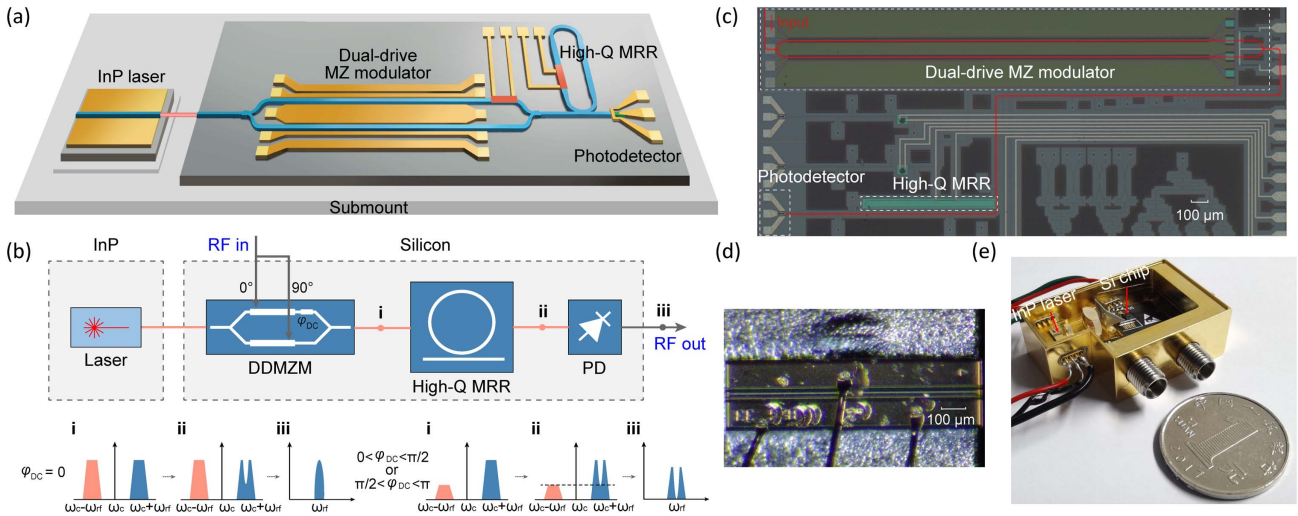

Fig. 1. (a) Schematic diagram of the hybrid integrated MPF. (b) The operation principles for the bandpass/band-stop switchable filtering response of the integrated MPF. (c) Optical image of the fabricated silicon chip. (d) Optical image of the InP laser diode chip. (e) Photograph of the packaged hybrid integrated MPF that comprises an InP laser, a silicon chip, and auxiliary microlenses and prism.

CMOS-compatible processes by Advanced Micro Foundry, as shown in Fig. 1(c). The footprint of the whole chip is about 1.34 mm × 3.18 mm. The DDMZM is based on a carrier-depletion scheme with a pair of 2.5 mm long electro-optical (EO) phase shifters. Traveling-wave electrodes are utilized to support high-speed operation. Two TiN microheaters with a length of 130 μm are placed on the two arms of the MZI to control the bias point of the DDMZM. The high-Q MRR is based on rib waveguides with a 90 nm slab and is designed to have an all-pass racetrack configuration with a free spectral range (FSR) of ~50 GHz. To improve the Q-factor, the width of straight waveguides is set as 2 μm for eliminating scattering loss from the rough sidewalls, while the width of bent waveguides (20 μm in radius) is 450 nm to enable low-loss bending. To avoid exciting high-order optical mode, 40 μm long adiabatic tapers are used for the connection of 2 μm waveguides and 450 nm waveguides. A TiN microheater is applied to tune the wavelength shift of the resonance peaks. The PD is designed as a vertical p-doped-intrinsic-n-doped (PIN) structure and realized by germanium (Ge) epitaxy growth technique. Besides, in order to monitor the optical signals at different positions of the on-chip optical link, several asymmetric optical couplers with a splitting ratio of 1:9 [40] are inserted to extract 10% power of the propagation light for monitoring.

The integrated light source used here is a commercially available InP DFB laser diode die (0.9 mm × 0.25 mm) based on a buried-heterostructure waveguide structure [see Fig. 1(d)], which has an emitting wavelength around 1552 nm and an output power of 95 mW. A thermoelectric cooler (TEC) is implemented to control and stabilize the operation temperature. The InP laser chip and the monolithic silicon chip were hybrid integrated with the help of micro-optics elements (see Appendix B) and assembled into a compact package, as shown in Fig. 1(e). The RF and DC pads on chip were wire-bonded to a custom-designed print circuit board (PCB) for electrical connections.

3. EXPERIMENTAL RESULTS

A. Characterization of Key Devices

The transmission spectrum of the high-Q MRR is presented in Fig. 2(a). The extracted full width at half maximum (FWHM) is 2.3 pm, corresponding to a loaded Q-factor of 6.7×10^5. The Lorentzian fitting shows that the intrinsic Q-factor and the average propagation loss are 1.63×10^6 and 0.41 dB/cm, respectively. Such a high Q-factor will enable the integrated MPF to realize highly selective filtering with a sub-GHz passband or stopband bandwidth. Figure 2(b) presents the phase response of the high-Q MRR within a resonance, which was measured by a high-resolution optical vector analysis method (Appendix C). It can be observed that the phase shift at the

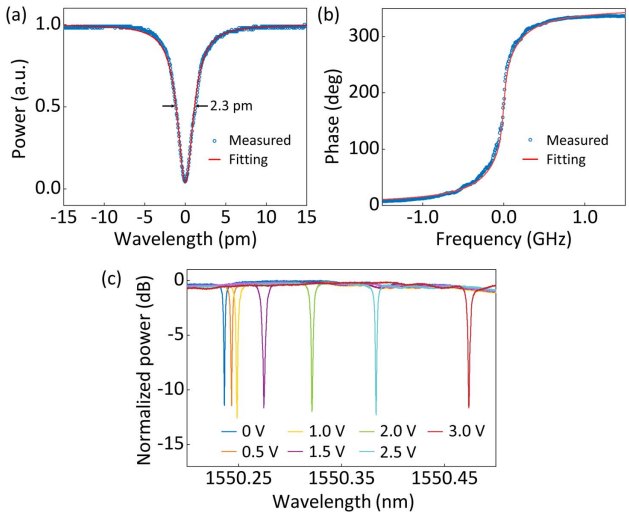

Fig. 2. (a) Measured transmission spectrum of the high-Q MRR. (b) Measured phase response within a resonance of the high-Q MRR. (c) Measured optical spectra with various DC voltages applied to the TiN microheater.

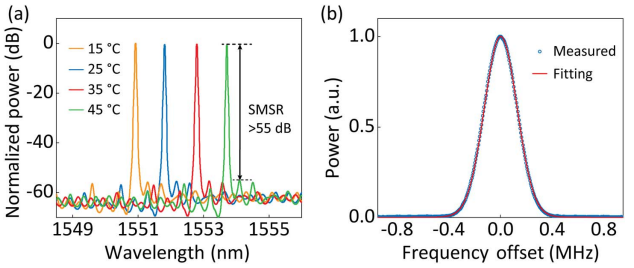

Fig. 3. (a) Measured output spectra of the InP-based laser chip under different operation temperatures. (b) DSH linewidth measurement (blue dots) and a Voigt curve fit (red line) show a 3 dB Lorentzian linewidth of 150 kHz.

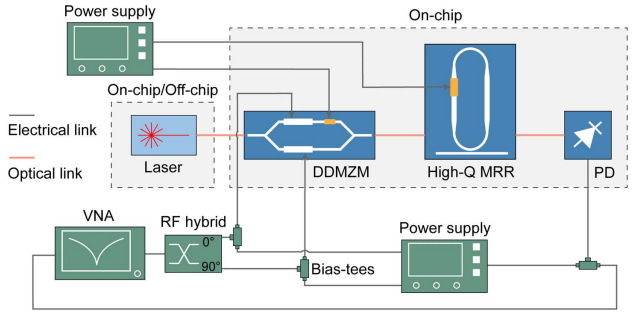

Fig. 4. Experimental setup to measure the band-stop/bandpass filtering response of the integrated MPF.

resonance frequency is nearly 180°, indicating the high-Q MRR is under the overcoupling state [41]. Thus, the bias phase φ_{DC} is required to be tuned to the range of $[\pi/2, \pi]$ for realizing a deep band-stop filter (Appendix A). The tunability of the optical spectrum was also evaluated, as shown in Fig. 2(c). By changing the DC voltages applied to the TiN microheater from 0 to 3 V, the resonance wavelength of the high-Q MRR can be continuously redshifted up to 0.24 nm (30 GHz).

Then, the performances of the active devices in this hybrid integrated MPF were evaluated. The output of the InP-based DFB laser was sent into an optical spectrum analyzer (OSA, Yokogawa 6370C) to characterize the laser spectrum, as seen in Fig. 3(a). The side mode suppression ratio is higher than 55 dB around 1552 nm. The linewidth of the laser was measured by a delayed self-heterodyne (DSH) method (Appendix D), which is extracted as narrow as 150 kHz, as shown in Fig. 3(b). For the DDMZM, the static insertion loss is ~4.6 dB, and the modulation efficiency is approximately 1.65 V · cm. The 3 dB EO modulation bandwidth was measured as 26.5 GHz at a reverse-bias voltage of 2.5 V. For the PD, a detection responsivity of ~0.8 A/W at 1550 nm was observed. The 3 dB optical-electro (OE) bandwidth was tested as large as 38 GHz under a bias voltage of 2 V. More detailed measurement results can be found in Appendix E. Thanks to the large bandwidths of both the DDMZM and PD, the integrated MPF is capable of supporting a rather wide operation frequency range.

B. Filtering Response

Using the setup shown in Fig. 4, two experiments for measuring the RF filtering response of the integrated MPF were performed. In the first experiment, the RF spectra were measured based on the monolithic silicon chip and an external light source (EXFO, T100S-HP). In this case, a CW light was generated by the external laser and injected into the silicon chip with a power of ~16 dBm, subtracting a coupling loss of 7 dB. Frequency-swept RF signals with 9.5 dBm power were provided by a vector network analyzer (VNA, Keysight N5247A) and divided by a 90° RF hybrid (Marki, QH-0440) to drive the two EO phase shifters of the DDMZM. Then, the recovered RF signals from the PD were sent back to the VNA to acquire the frequency response of the integrated MPF. During the measurement, the input/output RF signals were connected to the bond pads of the silicon chip through high-speed microwave probes (Cascade Microtech, ACP40). The desired reverse bias voltages of the DDMZM and PD were provided by a multichannel DC power supply (Keysight, E36312A) and combined with RF signals using bias-tees (SHF, BT65D). In addition, for thermally tuning the DC bias phase φ_{DC} of the DDMZM and the resonance wavelength of the high-Q MRR, another DC power supply (Keysight, E36312A) was adopted.

The frequency response of the integrated MPF operating as a band-stop filter was measured first. A resonance notch at 1552.27 nm was selected to filter the upper sideband of the AS-DSB optical signals. Through precisely controlling the DC bias phase of the DDMZM to enable full cancellation of two beat sidebands, a deep RF frequency notch was realized at ~3 GHz. In order to validate the frequency tunability, the resonance wavelength of high-Q MRR was tuned through a microheater. As shown in Fig. 5(a), with the electrical power applied to the microheater sweeping within 0 to 17.4 mW, the center frequency of the notch band can be continuously tuned from 3 to 25 GHz (S-band to K-band). It should be noted that the lower-frequency limit is restricted by the valid operation range of the RF hybrid, while the upper frequency

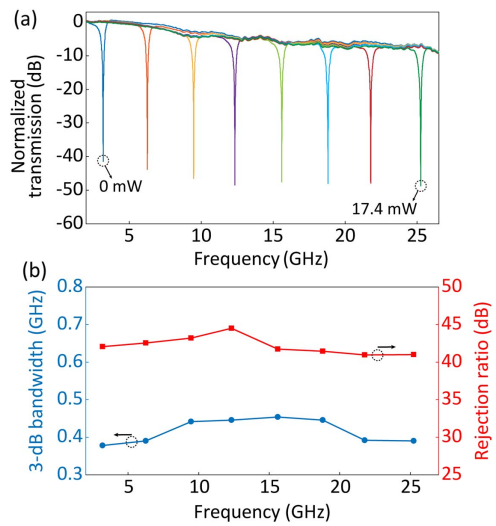

Fig. 5. (a) Measured RF responses of the band-stop filtering at various center frequencies. (b) 3 dB bandwidths and rejection ratios are plotted versus RF frequencies.

limit is determined by the half-FSR of the high-Q MRR. Therefore, the frequency tunable range could be flexibly extended via further optimization. Figure 5(b) depicts the 3 dB bandwidths and rejection ratios as functions of RF frequencies. It can be observed that the rejection ratios maintain a high level of >40 dB over the entire frequency tunable range (3 to 25 GHz), and the 3 dB bandwidths are extracted within 380 to 450 MHz. The long-term stability for maintaining these high performances was also evaluated and is given in Appendix F.

Next, the integrated MPF operating as a bandpass filter was demonstrated and evaluated. By setting φ_{DC} equal to zero, the filter function was rapidly switched to bandpass filtering with a response time of ~48 μs (Appendix G). Figure 6(a) illustrates the frequency responses of the bandpass filtering. As can be seen, the center frequency of the passband can be adjusted in a wide frequency range of 3 to 21 GHz with the electrical power changing from 0 to 15.1 mW. Figure 6(b) represents the 3 dB bandwidths and rejection ratios versus different RF frequencies. The 3 dB bandwidths are located at 360 to 470 MHz and are in good conformity with those of the band-stop filtering. In parallel, the rejection ratios are >10 dB over the entire frequency tunable range (3 to 21 GHz), which are poorer than those in Fig. 5(b). The reduced rejection ratios arise from the insufficient cancellation between the ±1st order sidebands, given that the ideal EPM relationship is difficult to be maintained over a broad frequency range, considering the phase unbalances originated from the RF hybrid, cables, and fabrication errors of devices.

In the second experiment, the filtering response was evaluated and validated experimentally based on the hybrid all-integrated MPF with package. That is, the InP chip-based laser was turned on, and the microwave signals were input/output of the packaged MPF module through the peripheral RF connectors. The other measurement settings remained unchanged compared with those in the first experiment. In this way, evident bandpass filtering and band-stop filtering profiles

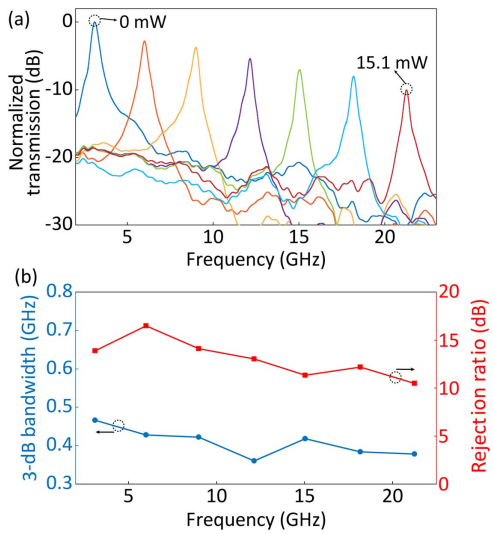

Fig. 6. (a) Measured RF responses of the bandpass filtering at different center frequencies. (b) 3 dB bandwidths and rejection ratios are plotted versus RF frequencies.

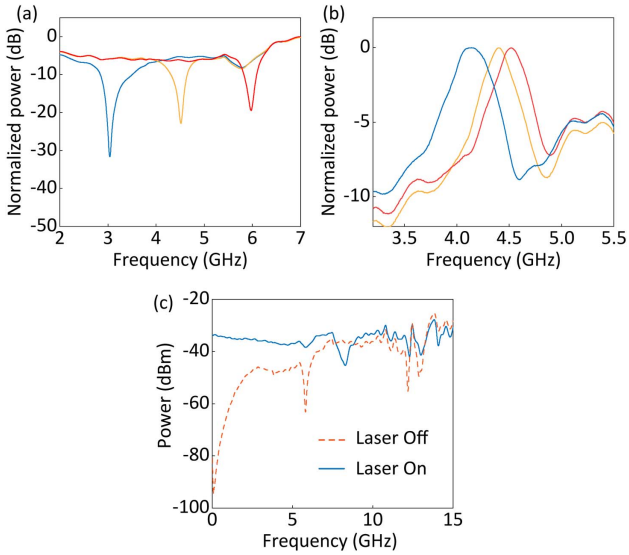

Fig. 7. Experimental results for the hybrid all-integrated MPF with package. (a) Measured RF spectra of the band-stop filtering. (b) Measured RF spectra of the bandpass filtering. (c) Measured S_{21} responses when the InP laser is turned off and turned on, respectively.

were also able to be observed, as shown in Fig. 7(a) and Fig. 7(b), respectively. However, the filtering functionalities are only valid across a limited frequency range, and the performance metrics are far worse than those achieved in Figs. 5 and 6. The noise power spectral density was also evaluated at 3 GHz with 2 mA generated photocurrent, which is around −151 dBm/Hz.

The damaged filtering performances are due to the severe internal RF crosstalk [23], mostly induced by the RF packaging operation. As seen in Fig. 7(c), when the chip-based InP laser is turned off and turned on, the two obtained S_{21} curves only have difference within a low frequency range (DC-6 GHz). This unexpected phenomenon is because the distance between the RF transmission lines for the DDMZM and PD is relatively small; even if no optical signal exists, a portion of microwave signal from the input RF lines (connected to DDMZM) will be directly coupled into the output RF lines (connected to PD) [42]. Furthermore, considering the inevitable alignment errors in lens assembly, the optical coupling loss between the InP laser and the silicon chip is large (12.3 dB, see Appendix B), which will be converted into the loss in the RF domain. Therefore, we could not access to the full filtering performances of the integrated MPF by this measurement approach.

Nevertheless, the proposed hybrid integration scheme to realize an all-integrated MPF is practicable. With further improvements in RF packaging and optical coupling, much higher filtering performances can be envisioned. For example, the RF crosstalk can be effectively eliminated by placing the RF pads of DDMZM and PD at opposite chip edges to have larger spatial distance in future tape-out. Based on our current chip layout, to fully exploit the truly entire functionalities of this integrated MPF, the setup of the first experiment was adopted in subsequent measurements.

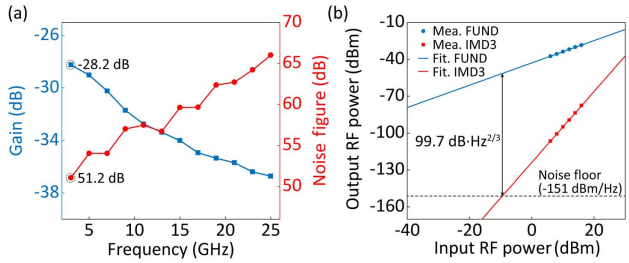

Fig. 8. (a) Measured RF link gain and noise figure over the whole tunable frequency range. (b) Measured power of the fundamental (FUND) component and the third-order intermodulation (IMD3) component versus different input RF power.

C. RF Link Performance

In addition to the filtering functionalities, the RF link performance is also an important issue, which should be considered for the integrated MPF, mainly including RF link gain, noise figure, and spurious-free dynamic range (SFDR) [43]. The link gain G is defined as the RF power ratio of the output signal to the input signal, which was measured by a VNA after calibration. For the noise figure (NF), the expression can be given by [5]

$$\mathrm{NF} = P_N - G + 174, \tag{1}$$

where P_N is the detected electrical noise power, mainly resulting from the relative-intensity noise of the laser and the shot noise and thermal noise of the on-chip PD. The P_N was extracted by measuring the RF power spectrum using an electrical spectrum analyzer (ESA, Keysight N9010B) at a resolution bandwidth of 1 Hz. Figure 8(a) displays the RF link gain and noise figure at various frequencies, which were both measured under band-stop filtering function. The maximum link gain reaches −28.2 dB at 3 GHz, which is corresponding to a noise figure of 51.2 dB. It can be seen that the link gain gradually drops with the increase of the RF frequency, arising from the inherent declines in RF responses of the DDMZM and PD.

In order to obtain the SFDR, a standard two-tone test was carried out. Two RF tones at 3 and 3.01 GHz were generated by two analog signal generators (ASGs, Keysight E8257D and Anritsu MG3695A), combined by an RF coupler, and then applied to the DDMZM. The RF tones are located at the passband of the integrated MPF. An ESA was used to study the RF spectrum detected by the on-chip PD. The powers of the fundamental components (FUND, 3 and 3.01 GHz) and the third-order intermodulation components (IMD3, 3.02 and 2.99 GHz) were extracted under different input RF power, as shown in Fig. 8(b). Given a measured noise floor of −151 dBm/Hz, the SFDR for IMD3 was calculated as 99.7 $\mathrm{dB \cdot Hz^{2/3}}$, which is higher than that of previous highly integrated MPFs [23,25] but still far from the target performance (>120 $\mathrm{dB \cdot Hz^{2/3}}$ [31]) required for practical applications. The promising strategies to improve the SFDR will be discussed later.

D. High-Resolution Switchable RF Filtering

To testify that our proposed integrated MPF holds the capacity to handle practical tasks in real-world RF systems, we performed high-resolution switchable RF filtering of analog signals toward two typical application scenarios. The first scenario is that the received signal of interest is accompanied by a spectrally closed strong interferer. In such case, the integrated MPF should operate as a highly selective notch filter to suppress the interferer for maximizing the signal-to-noise ratio (SNR) [28]. In the demonstration experiment, a targeted signal at 15 GHz and an unwanted interferer at 15.25 GHz were provided by two ASGs and combined by an RF coupler and then act as input of the integrated MPF. After passing through the integrated MPF, the output RF spectrum was measured and analyzed by an ESA. As shown in Fig. 9(a), if the inputs are located away from the filter stopband, the targeted signal has a power of −42.3 dBm and the interferer has −31.8 dBm (10.5 dB stronger than signal). Subsequently, the stop band of the integrated MPF is tuned to suppress the interferer. The filtered RF spectrum is depicted in Fig. 9(b). It can be observed that the interferer is drastically rejected with an ultrahigh suppression ratio of 43 dB, while the desired signal is well retained with a low attenuation of only 3.6 dB.

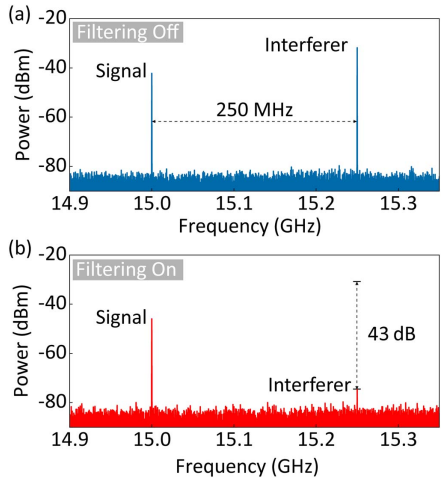

Fig. 9. High-resolution RF filtering using the integrated MPF as a band-stop filter. The input contains two frequency components (signal at 15 GHz and interferer at 15.25 GHz). (a) Measured RF spectrum when the input is located outside the stopband. (b) Measured RF spectrum when the interferer is filtered by the stop band.

The second scenario is that multiple frequency bands simultaneously exist in RF environments, while each time only one channel signal is supposed to be isolated and processed. Under this situation, a center-frequency tunable bandpass filter is needed to carry out the channel selection [30]. To simulate this real-scene, two RF signals at 11 GHz as channel 1 and at 13 GHz as channel 2 with equal power were generated to serve as input of the integrated MPF. The integrated MPF was switched to the bandpass operation mode by adjusting φ_{DC}. By tuning the center frequency of the passband, we can flexibly select one channel to pass through, while the other channel is blocked. As shown in Fig. 10(a), when the center frequency of the filter passband is tuned to 11 GHz, the signal at channel 1 passes, while the signal at channel 2 is rejected. The power difference between channel 1 and channel 2 is up to 19 dB. If the filter passband is shifted to 13 GHz, in this way, the signal at

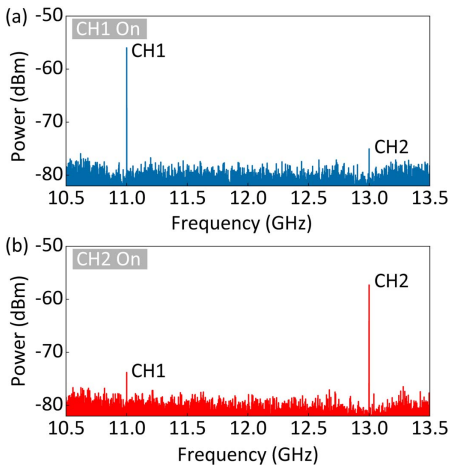

Fig. 10. High-resolution RF filtering using the integrated MPF as a bandpass filter. The input contains two channel signals, i.e., channel 1 (CH1, 11 GHz) and channel 2 (CH2, 13 GHz). (a) Measured RF spectrum when the CH1 is located at the passband. (b) Measured RF spectrum when the CH2 is located at the passband.

channel 2 is selected, while the signal at channel 1 is effectively blocked with a suppression ratio of 16.5 dB, as depicted in Fig. 10(b).

These results above highlight the advanced filtering performances of the integrated MPF, in combinations of high operation frequency, high-resolution selectivity, and large rejection ratio. Meanwhile, the filtering response is proved to be agilely switched between the band-stop and bandpass for coping with dissimilar type of signals, which is expected to be quite useful for reducing RF system volumes and improving versatility.

4. DISCUSSION

To benchmark the overall performance of the proposed integrated MPF in this work, we make a comparison among state-of-the-art integrated MPFs and electronic microwave filters, as displayed in Table 1. First, we observe that the spectral resolution and suppression ratio achieved in our work are competitive with those of electronic microwave filters, while the frequency tunable range is much broader thanks to the intrinsic advantages of microwave photonics (MWP) technology. Second, for all the integrated MPFs with high integration degree (≥50%), our work shows the most advanced filtering performances in combination of a broad frequency tunable range (from S-band to K-band), a narrow 3 dB bandwidth (360 to 470 MHz), and a high rejection ratio (>40 dB), which are comparable to or even better than other integrated MPFs with low integration degree (≤25%) and discrete MPFs [10–13]. Meanwhile, the filter type can be flexibly and rapidly switched (~48 μs response time) between bandpass and band-stop, which holds exciting benefits for the current dynamically changing RF environment. More importantly, compared with the InP monolithic solution to realize 100% photonic integration [23], our hybrid integration approach combines the foundry-enabled low-loss silicon photonics platform and readily processed InP chip-scale light sources and, therefore, is more cost-effective, provides a higher level of scalability, and offers new opportunities to overcome the limitations of individual material platforms [38].

Because the achieved filtering performances are capable of coping with the practical tasks, the remaining hurdle is the RF link performance. The lowest RF-to-RF insertion loss of our proposed integrated MPF is 28.2 dB, which is much larger than that of electronic filters. There are two major factors

Table 1. Performance Comparison of State-of-the-Art Integrated MPFs and Electronic Microwave Filters

Platform	Integrated Devices	Integration Degree	Filter Type	Tunable Range (GHz)	3 dB Bandwidth (GHz)	Rejection Ratio (dB)	SFDR ($dB \cdot Hz^{2/3}$)	Gain (dB)	Noise Figure (dB)
Electronic [44]	N/A	N/A	Band-stop	4–6/6.3–11.4	0.035/0.306	>35	N/A	–2	N/A
Electronic [45]	N/A	N/A	Bandpass	5.07–5.53	0.46	>30	N/A	–1.5	N/A
As_2S_3 [22]	Optical filter	25%	Bandpass	1–20	0.02–0.35	>40	N/A	–5	N/A
As_2S_3 [46]	Optical filter	25%	Band-stop	0–15	3	>40	96.5	–10.1	27.1
InP [17]	Optical filter	25%	Bandpass	0–27	1.9–5.4	32	86.3	N/A	23.2
Si_3N_4 [47]	Optical filter	25%	Bandpass/ Band-stop	4–25	4.54–9.72/ 3.65–6.35	>20	N/A	–10	N/A
Si_3N_4 [48]	Optical filter	25%	Band-stop	0–12	0.15–0.35	>50	116	8	15.6
SOI [15]	Optical filter	25%	Band-stop	2–15	0.91	>30	N/A	N/A	N/A
SOI [16]	Optical filter	25%	Bandpass	2–18.4	0.17	26.5	N/A	–42	N/A
SOI [49]	Optical filter	25%	Bandpass	4–10	0.0035	70	90.3	–17.3	56.7
SOI [26]	Optical filter and PD	50%	Bandpass	0–25	5.3–19.5	>30	N/A	N/A	N/A
SOI [25]	Modulator, optical filter, and PD	75%	Bandpass	3–10	1.93	15	92.4	–38.9	N/A
SOI [42]	Modulator, optical filter, and PD	75%	Bandpass/ Band-stop	9–21/5–25	N/A	>15/ >30	N/A	N/A	N/A
InP[a] [23]	Laser, modulator, optical filter, and PD	100%	Low-pass	0–6	2.5–5.5	30	81.4	–20	N/A
InP + SOI[b] (this work)	Laser, modulator, optical filter, and PD	100%	Bandpass/ Band-stop	3–21/3–25	0.36–0.47/ 0.38–0.45	>10/ >40	99.7	–28.2	51.2

[a]The performance metrics are evaluated experimentally in 75% photonic integration, where the laser, optical filter, and modulator are on-chip and the PD is off-chip.
[b]The performance metrics are evaluated experimentally in 75% photonic integration, where the modulator, optical filter, and PD are on-chip and the laser is off-chip.

responsible for the RF insertion loss and they are the high optical link loss and the limited E/O and O/E conversion efficiencies. Hence, the RF insertion loss is possible to be greatly decreased if these two issues could be effectively solved. For reducing the optical link loss, the hybrid integration approach by micro-optics adopted in this work can be replaced by a more efficient photonic wire-bonding technique to achieve an ultra-low coupling loss of 0.4 dB [35]. The main on-chip insertion loss derived from the silicon MZ modulator can also be reduced through optimization of the doped region in the waveguide to avoid unnecessary free-carrier absorption [50]. Alternatively, chip-based III-V/Si optical amplifiers could be considered for compensating the propagation loss [51]. For improving the efficiencies of E/O and O/E conversion, a highly efficient silicon MZ modulator with a U-shaped PN junction has recently been demonstrated to have a low half-wave voltage of only 1.7 V [52], and a Ge-Si PD based on whispering gallery structure has reached a high responsivity of 1.04 A/W [53]. Furthermore, utilizing the novel cascaded MRR scheme reported in Ref. [54] will also yield an improvement of link gain. In addition to the optimization of optical devices, the RF loss can also be compensated in the electrical domain by placing a low-noise RF amplifier at the input to the modulator.

Additionally, the SFDR of this integrated MPF is limited by the intrinsic nonlinearity of the silicon modulator, which may also need further promotion. Prospects to improve the SFDR of the silicon modulator have been illustrated by linearization approaches [55–57]. For example, via manipulating power distribution of a dual-parallel MZ silicon modulator, the SFDR for IMD3 has been improved to an ultrahigh value of 120 dB · $\mathrm{Hz}^{6/7}$ [57]. The reduction of the RF insertion loss discussed above is beneficial to improve the SFDR as well.

Looking forward, with recent developments on large-bandwidth (>60 GHz) silicon modulators [58] and PDs [59], assisted by optimized silicon MRRs with ultrahigh Q-factor (loaded $Q > 1.3 \times 10^6$) and large FSR (>100 GHz) [60], a hybrid integrated MPF featuring an operation frequency extending to the mm wave region (30 to 300 GHz) with a spectral resolution of ~100 MHz is within reach. In parallel, the serious internal RF crosstalk arising from the packaging processes can also be eliminated by proper redesign of chip layout and PCB. Therefore, we can envision that our proposed integrated MPF will find important and immediate applications in various RF systems. Moreover, our hybrid design can be easily expanded to other MWP functional systems, such as optoelectronic oscillators [61] and instantaneous frequency measurements [62].

5. CONCLUSION

In summary, we have demonstrated an all-integrated high-performance MPF with bandpass/band-stop switchable filtering response, through hybrid InP and Si integration. This integrated MPF achieves high filtering performances in combination of a broad frequency tunable range, a narrow 3 dB bandwidth, and a large rejection ratio as well as agile (~48 μs) switchable filtering function, which is superior to any highly integrated MPF reported before. For the band-stop filtering, a frequency tunable range of 3 to 25 GHz and a 3 dB bandwidth of 380 to 450 MHz are obtained, along with a high rejection ratio of >40 dB. For the bandpass filtering, the frequency tunable range and 3 dB bandwidth are 3 to 21 GHz and 360 to 470 MHz, respectively. With respect to RF link performances, an RF gain of −28.2 dB, a noise figure of 51.2 dB, and a spurious-free dynamic range of 99.7 dB · $\mathrm{Hz}^{2/3}$ are achieved. To validate the capacity of this integrated MPF toward real-world application scenes, high-resolution RF filtering of realistic signals for both interference suppression and channel selection is carried out. It is anticipated that the hybrid integrated MPF demonstrated here could greatly advance the development of various RF application fields ranging from radar to wireless communication in near-future, for accessing to larger frequency-band, smaller footprint, and higher efficiency.

APPENDIX A: PRINCIPLE OF SWITCHABLE FILTERING

As shown in Fig. 1(b), an optical carrier with an angular frequency of ω_c from the InP CW laser is injected into the silicon chip and is then routed to the DDMZM. A microwave signal $V_{\mathrm{rf}} \cos(\omega_{\mathrm{rf}} t)$ is applied to the DDMZM by a 90° RF hybrid. In this way, a $\pi/2$ relative phase difference is introduced for the two EO phase shifters. Under small-signal modulation and neglecting the high-order sidebands (≥2nd), the optical signal at the output of the DDMZM [position i in Fig. 1(b)] can be expressed as Eq. (A1) [13,14]:

$$E_1(t) = E_l e^{i[(\omega_c - \omega_{\mathrm{rf}})t + 3\pi/4]} + E_c e^{i\omega_c t} + E_u e^{i[(\omega_c + \omega_{\mathrm{rf}})t + \pi/4]}, \tag{A1}$$

where E_c, E_l, and E_u denote the amplitudes of the optical carrier, the lower −1st sideband, and the upper +1st sideband, which can be given by specific forms shown in Eq. (A2) [14]:

$$\begin{aligned} E_c &= E_0 e^{i\varphi_{\mathrm{DC}}/2} J_0(\beta) \cos(\varphi_{\mathrm{DC}}/2), \\ E_l &= E_0 e^{i\varphi_{\mathrm{DC}}/2} J_1(\beta) \cos(\varphi_{\mathrm{DC}}/2 + \pi/4), \\ E_u &= E_0 e^{i\varphi_{\mathrm{DC}}/2} J_1(\beta) \cos(\varphi_{\mathrm{DC}}/2 - \pi/4), \end{aligned} \tag{A2}$$

where E_0 is the amplitude of the input optical carrier, φ_{DC} is the static phase difference of the DDMZM, J_n is the nth-order Bessel functions of the first kind, $\beta = \pi V_{\mathrm{rf}}/\sqrt{2} V_\pi$ is the modulation index, and V_π is the half-wave voltage of the DDMZM. From Eqs. (A1) and (A2), it can be seen that the properties of the modulated optical signals can be easily adjusted by tuning φ_{DC}, providing an important degree of freedom to implement various filter schemes. The microwave-modulated signal is then tailored by the high-Q MRR. The processed optical signal [position ii in Fig. 1(b)] can be written as shown in Eq. (A3):

$$\begin{aligned} E_2(t) = {} & H(\omega_c - \omega_{\mathrm{rf}}) E_l e^{i[(\omega_c - \omega_{\mathrm{rf}})t + 3\pi/4]} + H(\omega_c) E_c e^{i\omega_c t} \\ & + H(\omega_c + \omega_{\mathrm{rf}}) E_u e^{i[(\omega_c + \omega_{\mathrm{rf}})t + \pi/4]}, \end{aligned} \tag{A3}$$

where $H(\omega)$ is the complex transfer function of the high-Q MRR. Assuming the upper sideband falls into the resonance notch, one can obtain $H(\omega_c - \omega_{\mathrm{rf}}) = H(\omega_c) = 1$ and $H(\omega_c + \omega_{\mathrm{rf}}) = H_{\mathrm{res}} e^{i\theta_{\mathrm{res}}}$. The H_{res} and θ_{res} represent the amplitude transmission and phase response caused by the

resonance of the high-Q MRR. Accordingly, Eq. (A3) can be simplified as below [Eq. (A4)]:

$$E_2(t) = E_l e^{i[(\omega_c-\omega_{\rm rf})t+3\pi/4]} + E_c e^{i\omega_c t} + H_{\rm res} E_u e^{i[(\omega_c+\omega_{\rm rf})t+\pi/4+\theta_{\rm res}]}. \quad \textbf{(A4)}$$

The $H_{\rm res}$ is determined by the extinction ratio of the resonance peak, and the $\theta_{\rm res}$ is related to the coupling state. The $\theta_{\rm res}$ is equal to 0 when the high-Q MRR is under-coupling while is equal to π under the overcoupling state [41]. Finally, the processed optical signal is detected by the PD. Ignoring the DC and small harmonic components, the generated photocurrent [position iii in Fig. 1(b)] can be given by Eq. (A5) [14]:

$$i_e(t) \propto E_c E_l \cos(\omega_{\rm rf} t - 3\pi/4) + H_{\rm res} E_c E_u \cos(\omega_{\rm rf} t + \pi/4 + \theta_{\rm res}). \quad \textbf{(A5)}$$

Combining Eqs. (A2) and (A5), it can be clearly seen that the recovered microwave signal at the output of the PD is varied with different $\varphi_{\rm DC}$, which can be used to switch the filtering response of the integrated MPF.

To implement a bandpass filter, the $\varphi_{\rm DC}$ should be tuned to 0 for producing the EPM scheme. In this case, the lower and upper sidebands have the same amplitude. If the high-Q MRR is not used, the beating signals between the carrier and two sidebands are out-of-phase and will fully cancel each other; thus, no photocurrent will be generated in the PD. However, once the upper sideband falls into the resonance notch of the high-Q MRR, the out-of-phase property will be broken; then, an RF passband can be obtained. This process is also well known as the phase modulation to intensity modulation (PM-IM) conversion [10].

To implement a band-stop filter, the $\varphi_{\rm DC}$ should be tuned to generate the AS-DSB scheme. In this situation, the amplitude of upper sideband is higher than that of the lower sideband. Meanwhile, the phase relationship of beating signals between the carrier and two sidebands can be out-of-phase or in-phase, when the value of $\varphi_{\rm DC}$ severally locates at the range of $[0, \pi/2]$ or $[\pi/2, \pi]$. In order to achieve a high RF stopband, the required value of $\varphi_{\rm DC}$ is decided by the coupling state of the high-Q MRR. If the high-Q MRR is under-coupling such that zero phase-shift occurs in the resonance notch, the $\varphi_{\rm DC}$ is supposed to be tuned to the range of $[0, \pi/2]$ to construct out-of-phase relationship. The notch of the high-Q MRR is utilized to partly suppress the upper sideband to make the amplitude of the filtered upper sideband equal to that of the lower sideband; thereby, a full cancellation of the two beat signals can be realized to result in a deep notch in the RF spectrum. In the same way, if the high-Q MRR is overcoupling such that a π phase-shift will produce in the resonance, the $\varphi_{\rm DC}$ should be tuned to $[\pi/2, \pi]$ to fulfill the full-cancellation condition.

APPENDIX B: HYBRID INTEGRATION OF THE InP LASER CHIP AND THE Si CHIP

In the hybrid integration process, the InP laser diode chip and the Si photonic chip were optically connected based on off-the-shelf micro-optics components. Figure 11(a) displays the designed free-space beam propagation using the commercial software LightTools. The light beam emitted from the InP laser chip is first collimated by a microlens (custom-designed, focal length 1.92 mm). Then, the light beam is refocused by a second microlens (Thorlabs A375-C, focal length 7.5 mm) to match the beam irradiance of the grating coupler (mode field diameter of ~9 μm) on the Si chip. Finally, a 45° microprism with silver reflective coating (90% reflectivity) is used to redirect the light toward the grating coupler. The Si chip is bonded at a PCB, tilted at 8° from horizontal to realize an optimal light incident angle for minimal coupling loss.

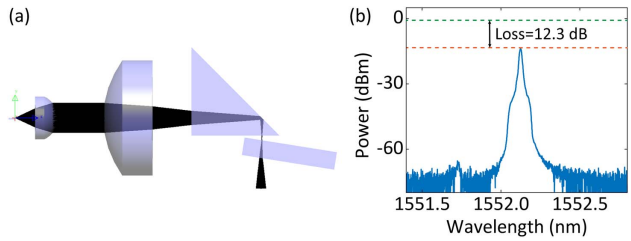

Fig. 11. (a) Beam propagation simulation for the hybrid integration of the InP laser and Si chip utilizing micro-optics. (b) Measured total coupling loss between these two chips. Green line: InP laser output subtracting all link propagation loss except coupling loss. Orange line: optical power measured from the monitor grating located behind the DDMZM.

A package scheme was developed for assembling this entire hybrid photonics system. First, the InP chip was mounted at an AlN ceramic submount, which has high thermal conductivity. Second, the PCB bonded with Si chip was placed at the metal substrate. Third, the microlens and prism were manually positioned and fixed, one by one in the order that light passes through them, as shown in Fig. 11(a). In this step, a vacuum-control gripper was used to hold and release the microlens and prism. The gripper was installed at a three-axis translational stage for manual alignment. Epoxy was then applied to the bottom of lenses and prism and was cured to provide sufficient support to the lenses and prism after confirming the optimal positions.

In order to evaluate the coupling efficiency between the InP laser and Si chip, the optical spectrum emitted from the monitor grating (1:9, located behind the DDMZM) was received by an OSA (Yokogawa 6370C), which has a power of −13.9 dBm (orange dot line), as shown in Fig. 11(b). While the power level (green dot line) is equal to the InP laser output (20 dBm), we subtract all link propagation loss except coupling loss (including DDMZM insertion loss of 4.6 dB, monitor splitting of 10 dB, and monitor-grating loss of 7 dB), which is at −1.6 dBm. Therefore, the total coupling loss between these two chips can be calculated at about 12.3 dB. The large coupling loss mainly arises from the alignment errors of the lens and prism in assembly, which could be further reduced using a higher-precision alignment system.

APPENDIX C: PHASE RESPONSE MEASUREMENT OF THE HIGH-Q MRR

The phase response of the high-Q MRR was characterized by a single sideband (SSB) modulation optical vector analysis method [63]. An optical carrier was generated from a tunable

laser (EXFO, T100S-HP), connected to a 40 GHz phase modulator (iXblue MPZ-LN-40) for producing a double-sideband (DSB) modulation signal. The wavelength of the optical carrier was set close to the resonance notch of the high-Q MRR. An optical wave-shaper (Finisar Waveshaper 4000S) was used as an optical bandpass filter to suppress the lower sideband to obtain the SSB modulation signal. Then, the SSB signal was sent into the high-Q MRR by an on-chip grating coupler. An EDFA was used to compensate the coupling loss and link loss. Finally, after passing through the high-Q MRR, the optical signal was converted to an electrical signal by a 50 GHz PD (Finisar, XPDV2150R). By sweeping the RF frequency of the microwave signal from a VNA (Keysight N5247A, 10 MHz–67 GHz), the optical phase response of the high-Q MRR was obtained.

APPENDIX D: LINEWIDTH MEASUREMENT OF THE InP LASER

The spectral linewidth of the integrated InP laser was characterized by a DSH approach. The laser output was split into two paths through a 3 dB coupler. One path was 80 MHz frequency shifted by an acousto-optic modulator (AOM, Gooch & Housego). The other path was delayed by a 10 km long-haul fiber. The light beams from these two paths were recombined again by another 3 dB coupler and then were injected into a PD (Finisar, XPDV2150R). The recovered electrical signal was detected by an ESA (Keysight 9010B). To verify the effectiveness of the DSH setup, we first independently measured the linewidth of a commercial laser, which is equal to the specified linewidth of 10 kHz.

APPENDIX E: PERFORMANCE DETAILS OF ON-CHIP MODULATOR AND PD

The performances of the on-chip modulator and PD in this integrated MPF were characterized through the preset monitor grating couplers. The EO S_{21} response of the modulator was measured by a VNA (Keysight N5247A, 10 MHz–67 GHz). As shown in Fig. 12(a), with the reverse-bias voltages applied to PN junctions changing from 0 to 2.5 V, the 3 dB EO bandwidth is gradually increased from 9.2 to 26.5 GHz. The modulation efficiency ($V_\pi L_\pi$) was measured using a 2 mm asymmetric Mach–Zehnder (MZ) modulator, which has the same design parameters as the device used in the integrated MPF. Figure 12(b) shows the transmission spectra under various DC voltages applied on the PN junction. The relative phase shift $\Delta\varphi$ can be extracted from Fig. 12(b) using Eq. (E1) as below [64]:

$$\Delta\varphi = \frac{2\pi \times \Delta\lambda}{\mathrm{FSR}}. \tag{E1}$$

The free spectral range (FSR) of the asymmetric MZ modulator is ~5.6 nm. At a reverse voltage of 3 V, the peak-wavelength shift is ~1.02 nm. Hence, the $V_\pi L_\pi$ is calculated as 1.65 V · cm.

For the PD, the OE S_{21} response of the PD was measured by a light-wave component analyzer (LCA, Keysight N4373D), as shown in Fig. 12(c). From the results, we can see that a maximum 3 dB operation bandwidth of nearly 38 GHz is achieved with a bias voltage of 2 V. The responsivity was characterized by testing the generated photocurrent using a high-accuracy source meter (Keithley 2611B) under corresponding injected optical power, as given in Fig. 12(d), which is calculated as ~0.8 A/W at 1550 nm.

APPENDIX F: LONG-TERM STABILITY OF THE FILTERING PERFORMANCES

To evaluate the long-term stability of the filtering performances, the rejection ratio and 3 dB bandwidth under band-stop filtering function are measured across a 1 h period. A TEC was adopted to stabilize the operation temperature at 23°C. The RF filtering spectra were acquired by a VNA (Keysight N5247A) with a 10 min interval, as shown in Fig. 13. It is obviously observed that both the rejection ratio and filtering linewidth are maintained at high level over the whole measurement period, though a certain degree of fluctuations was produced. Specifically, the average rejection ratios are located at the range of 39 to 44 dB, and the filtering bandwidths are located at 0.4 to 0.45 GHz. The major source of instability for the rejection ratio is the bias drift of the

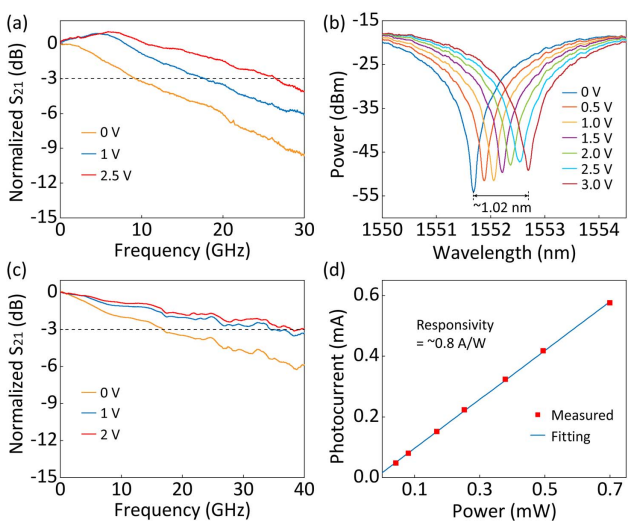

Fig. 12. (a) Measured S_{21} responses of the modulator. (b) Transmission spectra of the MZ modulator under different voltages. (c) Measured S_{21} responses of the PD. (d) The tested responsivity of the PD.

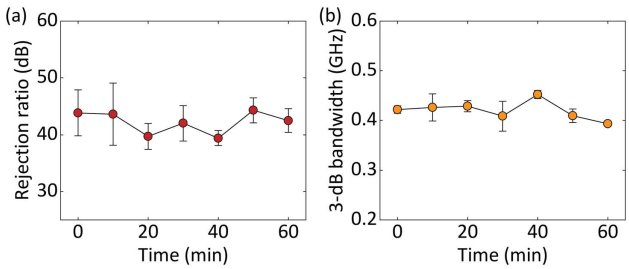

Fig. 13. (a) Measurement of the band-stop filter rejection ratio over 1 h continuous operation. (b) Measurement of the 3 dB bandwidth over 1 h continuous operation.

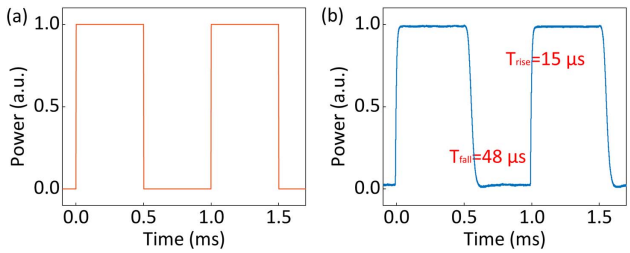

Fig. 14. Time-domain measurement of the TiN microheater placed on the DDMZM. (a) Temporal waveform of the applied square-wave electrical signal. (b) Measured temporal response with a rise/fall time of 15 and 48 μs.

DDMZM, which in turn causes the full-cancellation condition to be not well satisfied. The slight fluctuation of the measured 3 dB bandwidth is mainly originated from the thermal effect on the Q-factor of MRR. Toward the specific applications that require rigorous performance stability in the near future, more precise temperature control or an active feedback compensation loop is a practicable solution for this problem.

APPENDIX G: RESPONSE TIME OF FILTER FUNCTION SWITCHING

The switching operation between the bandpass and band-stop filter function is realized by changing the phase difference of the DDMZM, using the TiN microheater placed on waveguides. As a consequence, the required time for switching operation is determined by the response speed of the TiN microheater. To characterize the transient response of this thermo-optic switching process, a 1 kHz square-wave electrical signal was generated by a function waveform generator (RIGOL, DG2102 250 MSa/s) to drive the microheater. The modulated optical signal was converted to an electrical signal by an InGaAs photodetector (Thorlabs DET08CFC/M) and then was received by a digital oscilloscope (RIGOL, DS7014 10 GSa/s). Figure 14 shows the input electrical signal and the obtained switching response. As can be seen in Fig. 14(b), the measured switching rise and fall times are 15 and 48 μs, respectively. Therefore, the fastest response time for filter function switching is about 48 μs.

Funding. National Natural Science Foundation of China (61635001, 62001010); National Key Research and Development Program of China (2020YFB2206100); Beijing Key Research and Development Project (Z191100004819006); China National Postdoctoral Program for Innovative Talents (BX20200017).

Acknowledgment. The authors thank Advanced Micro Foundry (AMF) for silicon device fabrication and Shenzhen PhotonX Technology Co., Ltd. for the support on packages.

Disclosures. The authors declare no conflicts of interest.

REFERENCES

1. S. Pan and Y. Zhang, "Microwave photonic radars," J. Lightwave Technol. **38**, 5450–5484 (2020).
2. C. Liu, J. Wang, L. Cheng, M. Zhu, and G.-K. Chang, "Key microwave-photonics technologies for next-generation cloud-based radio access networks," J. Lightwave Technol. **32**, 3452–3460 (2014).
3. J. Hervás, A. L. Ricchiuti, W. Li, N. H. Zhu, C. R. Fernández-Pousa, S. Sales, M. Li, and J. Capmany, "Microwave photonics for optical sensors," IEEE J. Sel. Top. Quantum Electron. **23**, 327–339 (2017).
4. Y. Xie, Z. Geng, L. Zhuang, M. Burla, C. Taddei, M. Hoekman, A. Leinse, C. G. Roeloffzen, K.-J. Boller, and A. J. Lowery, "Programmable optical processor chips: toward photonic RF filters with DSP-level flexibility and mHz-band selectivity," Nanophotonics **7**, 421–454 (2018).
5. Y. Liu, A. Choudhary, D. Marpaung, and B. J. Eggleton, "Integrated microwave photonic filters," Adv. Opt. Photon. **12**, 485–555 (2020).
6. S. Dang, O. Amin, B. Shihada, and M.-S. Alouini, "What should 6G be?" Nat. Electron. **3**, 20–29 (2020).
7. B. Zong, C. Fan, X. Wang, X. Duan, B. Wang, and J. Wang, "6G technologies: key drivers, core requirements, system architectures, and enabling technologies," IEEE Veh. Technol. Mag. **14**, 18–27 (2019).
8. W. Peng and I. Hunter, "Electronically tunable filters," IEEE Microw. Mag. **10**, 46–54 (2009).
9. J. Capmany and D. Novak, "Microwave photonics combines two worlds," Nat. Photonics **1**, 319–330 (2007).
10. J. Yao, "Photonics to the rescue: a fresh look at microwave photonic filters," IEEE Microw. Mag. **16**, 46–60 (2015).
11. F. Zeng and J. Yao, "All-optical bandpass microwave filter based on an electro-optic phase modulator," Opt. Express **12**, 3814–3819 (2004).
12. W. Li, M. Li, and J. Yao, "A narrow-passband and frequency-tunable microwave photonic filter based on phase-modulation to intensity-modulation conversion using a phase-shifted fiber Bragg grating," IEEE Trans. Microw. Theory Tech. **60**, 1287–1296 (2012).
13. W. Zhang and R. A. Minasian, "Switchable and tunable microwave photonic Brillouin-based filter," IEEE Photon. J. **4**, 1443–1455 (2012).
14. X. Han and J. Yao, "Bandstop-to-bandpass microwave photonic filter using a phase-shifted fiber Bragg grating," J. Lightwave Technol. **33**, 5133–5139 (2015).
15. M. S. Rasras, K.-Y. Tu, D. M. Gill, Y.-K. Chen, A. E. White, S. S. Patel, A. Pomerene, D. Carothers, J. Beattie, M. Beals, J. Michel, and L. C. Kimerling, "Demonstration of a tunable microwave-photonic notch filter using low-loss silicon ring resonators," J. Lightwave Technol. **27**, 2105–2110 (2009).
16. H. Qiu, F. Zhou, J. Qie, Y. Yao, X. Hu, Y. Zhang, X. Xiao, Y. Yu, J. Dong, and X. Zhang, "A continuously tunable sub-gigahertz microwave photonic bandpass filter based on an ultra-high-Q silicon microring resonator," J. Lightwave Technol. **36**, 4312–4318 (2018).
17. E. J. Norberg, R. S. Guzzon, J. S. Parker, L. A. Johansson, and L. A. Coldren, "Programmable photonic microwave filters monolithically integrated in InP–InGaAsP," J. Lightwave Technol. **29**, 1611–1619 (2011).
18. M. Burla, L. R. Cortés, M. Li, X. Wang, L. Chrostowski, and J. Azaña, "Integrated waveguide Bragg gratings for microwave photonics signal processing," Opt. Express **21**, 25120–25147 (2013).
19. X. Xue, Y. Xuan, H.-J. Kim, J. Wang, D. E. Leaird, M. Qi, and A. M. Weiner, "Programmable single-bandpass photonic RF filter based on Kerr comb from a microring," J. Lightwave Technol. **32**, 3557–3565 (2014).
20. X. Xu, M. Tan, J. Wu, T. G. Nguyen, S. T. Chu, B. E. Little, R. Morandotti, A. Mitchell, and D. J. Moss, "Advanced adaptive photonic RF filters with 80 taps based on an integrated optical micro-comb source," J. Lightwave Technol. **37**, 1288–1295 (2019).
21. D. Marpaung, B. Morrison, M. Pagani, R. Pant, D.-Y. Choi, B. Luther-Davies, S. J. Madden, and B. J. Eggleton, "Low-power, chip-based stimulated Brillouin scattering microwave photonic filter with ultrahigh selectivity," Optica **2**, 76–83 (2015).
22. M. Garrett, Y. Liu, P. Ma, D.-Y. Choi, S. J. Madden, and B. J. Eggleton, "Low-RF-loss and large-rejection reconfigurable Brillouin-based RF photonic bandpass filter," Opt. Lett. **45**, 3705–3708 (2020).
23. J. S. Fandiño, P. Muñoz, D. Doménech, and J. Capmany, "A monolithic integrated photonic microwave filter," Nat. Photonics **11**, 124–129 (2017).
24. M. H. Idjadi and F. Aflatouni, "Nanophotonic phase noise filter in silicon," Nat. Photonics **14**, 234–239 (2020).

25. W. Zhang and J. Yao, "On-chip silicon photonic integrated frequency-tunable bandpass microwave photonic filter," Opt. Lett. **43**, 3622–3625 (2018).
26. L. Xu, J. Hou, H. Tang, Y. Yu, Y. Yu, X. Shu, and X. Zhang, "Silicon-on-insulator-based microwave photonic filter with widely adjustable bandwidth," Photon. Res. **7**, 110–115 (2019).
27. R. W. Ridgway, C. L. Dohrman, and J. A. Conway, "Microwave photonics programs at DARPA," J. Lightwave Technol. **32**, 3428–3439 (2014).
28. E. J. Naglich, J. Lee, D. Peroulis, and W. J. Chappell, "A tunable bandpass-to-bandstop reconfigurable filter with independent bandwidths and tunable response shape," IEEE Trans. Microwave Theory Tech. **58**, 3770–3779 (2010).
29. J. Lee, E. J. Naglich, H. H. Sigmarsson, D. Peroulis, and W. J. Chappell, "New bandstop filter circuit topology and its application to design of a bandstop-to-bandpass switchable filter," IEEE Trans. Microwave Theory Tech. **61**, 1114–1123 (2013).
30. R. A. Minasian, "Ultra-wideband and adaptive photonic signal processing of microwave signals," IEEE J. Quantum Electron. **52**, 0600813 (2015).
31. D. Marpaung, J. Yao, and J. Capmany, "Integrated microwave photonics," Nat. Photonics **13**, 80–90 (2019).
32. J. Kim, S. Aghaeimeibodi, J. Carolan, D. Englund, and E. Waks, "Hybrid integration methods for on-chip quantum photonics," Optica **7**, 291–308 (2020).
33. Y. Gao, J.-C. Lo, S. Lee, R. Patel, L. Zhu, J. Nee, D. Tsou, R. Carney, and J. Sun, "High-power, narrow-linewidth, miniaturized silicon photonic tunable laser with accurate frequency control," J. Lightwave Technol. **38**, 265–271 (2020).
34. B. Snyder, B. Corbett, and P. O'Brien, "Hybrid integration of the wavelength-tunable laser with a silicon photonic integrated circuit," J. Lightwave Technol. **31**, 3934–3942 (2013).
35. M. R. Billah, M. Blaicher, T. Hoose, P.-I. Dietrich, P. Marin-Palomo, N. Lindenmann, A. Nesic, A. Hofmann, U. Troppenz, M. Moehrle, S. Randel, W. Freude, and C. Koos, "Hybrid integration of silicon photonics circuits and InP lasers by photonic wire bonding," Optica **5**, 876–883 (2018).
36. M. Blaicher, M. R. Billah, J. Kemal, T. Hoose, P. Marin-Palomo, A. Hofmann, Y. Kutuvantavida, C. Kieninger, P.-I. Dietrich, M. Lauermann, S. Wolf, U. Troppenz, M. Moehrle, F. Merget, S. Skacel, J. Witzens, S. Randel, W. Freude, and C. Koos, "Hybrid multi-chip assembly of optical communication engines by *in situ* 3D nano-lithography," Light Sci. Appl. **9**, 71 (2020).
37. A. Novack, M. Streshinsky, T. N. Huynh, T. Galfsky, and M. Hochberg, "A silicon photonic transceiver and hybrid tunable laser for 64 Gbaud coherent communication," in *Optical Fiber Communication Conference* (2018), paper Th4D.4.
38. A. W. Elshaari, W. Pernice, K. Srinivasan, O. Benson, and V. Zwiller, "Hybrid integrated quantum photonic circuits," Nat. Photonics **14**, 285–298 (2020).
39. D. T. Spencer, T. Drake, T. C. Briles, J. Stone, L. C. Sinclair, C. Fredrick, Q. Li, D. Westly, B. R. Ilic, and A. Bluestone, "An optical-frequency synthesizer using integrated photonics," Nature **557**, 81–85 (2018).
40. Q. Deng, L. Liu, X. Li, and Z. Zhou, "Arbitrary-ratio 1×2 power splitter based on asymmetric multimode interference," Opt. Lett. **39**, 5590–5593 (2014).
41. W. Bogaerts, P. De Heyn, T. Van Vaerenbergh, K. De Vos, S. Kumar Selvaraja, T. Claes, P. Dumon, P. Bienstman, D. Van Thourhout, and R. Baets, "Silicon microring resonators," Laser Photon. Rev. **6**, 47–73 (2012).
42. X. Guo, Y. Liu, T. Yin, B. Morrison, M. Pagani, O. Daulay, W. Bogaerts, B. J. Eggleton, A. Casas-Bedoya, and D. Marpaung, "Versatile silicon microwave photonic spectral shaper," APL Photon. **6**, 036106 (2021).
43. Y. Liu, D. Marpaung, A. Choudhary, J. Hotten, and B. J. Eggleton, "Link performance optimization of chip-based Si_3N_4 microwave photonic filters," J. Lightwave Technol. **36**, 4361–4370 (2018).
44. E. J. Naglich, A. C. Guyette, and D. Peroulis, "High-Q intrinsically-switched quasi-absorptive tunable bandstop filter with electrically-short resonators," in *IEEE MTT-S International Microwave Symposium (IMS)* (IEEE, 2014), pp. 1–4.
45. A. Boutejdar, A. Ibrahim, and W. Ali, "Design of compact size and tunable band pass filter for WLAN applications," Electron. Lett. **52**, 1996–1997 (2016).
46. Y. Liu, A. Choudhary, G. Ren, K. Vu, B. Morrison, A. Casas-Bedoya, T. G. Nguyen, D.-Y. Choi, P. Ma, A. Mitchell, S. J. Madden, D. Marpaung, and B. J. Eggleton, "Integration of Brillouin and passive circuits for enhanced radio-frequency photonic filtering," APL Photon. **4**, 106103 (2019).
47. H. Yang, J. Li, P. Zheng, G. Hu, B. Yun, and Y. Cui, "A stopband and passband switchable microwave photonic filter based on integrated dual ring coupled Mach-Zehnder interferometer," IEEE Photon. J. **11**, 5502608 (2019).
48. Y. Liu, J. Hotten, A. Choudhary, B. J. Eggleton, and D. Marpaung, "All-optimized integrated RF photonic notch filter," Opt. Lett. **42**, 4631–4634 (2017).
49. S. Gertler, E. A. Kittlaus, N. T. Otterstrom, and P. T. Rakich, "Tunable microwave-photonic filtering with high out-of-band rejection in silicon," APL Photon. **5**, 096103 (2020).
50. G. T. Reed, G. Z. Mashanovich, F. Y. Gardes, M. Nedeljkovic, Y. Hu, D. J. Thomson, K. Li, P. R. Wilson, S.-W. Chen, and S. S. Hsu, "Recent breakthroughs in carrier depletion based silicon optical modulators," Nanophotonics **3**, 229–245 (2014).
51. K. Van Gasse, R. Wang, and G. Roelkens, "27 dB gain III–V-on-silicon semiconductor optical amplifier with >17 dBm output power," Opt. Express **27**, 293–302 (2019).
52. G. Zhou, L. Zhou, Y. Guo, S. Chen, L. Lu, L. Liu, and J. Chen, "32 Gb/s OOK and 64 Gb/s PAM-4 modulation using a single-drive silicon Mach–Zehnder modulator with 2 V drive voltage," IEEE Photon. J. **11**, 6603610 (2019).
53. Z. Su, E. S. Hosseini, E. Timurdogan, J. Sun, M. Moresco, G. Leake, T. N. Adam, D. D. Coolbaugh, and M. R. Watts, "Whispering gallery germanium-on-silicon photodetector," Opt. Lett. **42**, 2878–2881 (2017).
54. Z. Zhu, Y. Liu, M. Merklein, O. Daulay, D. Marpaung, and B. J. Eggleton, "Positive link gain microwave photonic bandpass filter using Si_3N_4-ring-enabled sideband filtering and carrier suppression," Opt. Express **27**, 31727–31740 (2019).
55. J. Ding, S. Shao, L. Zhang, X. Fu, and L. Yang, "Method to improve the linearity of the silicon Mach-Zehnder optical modulator by doping control," Opt. Express **24**, 24641–24648 (2016).
56. Y. Tao, H. Shu, M. Jin, X. Wang, L. Zhou, and W. Zou, "Numerical investigation of the linearity of graphene-based silicon waveguide modulator," Opt. Express **27**, 9013–9031 (2019).
57. Q. Zhang, H. Yu, P. Xia, Z. Fu, X. Wang, and J. Yang, "High linearity silicon modulator capable of actively compensating input distortion," Opt. Lett. **45**, 3785–3788 (2020).
58. H. Zhang, M. Li, Y. Zhang, D. Zhang, Q. Liao, J. He, S. Hu, B. Zhang, L. Wang, X. Xiao, N. Qi, and S. Yu, "800 Gbit/s transmission over 1 km single-mode fiber using a four-channel silicon photonic transmitter," Photon. Res. **8**, 1776–1782 (2020).
59. Y. Ding, Z. Cheng, X. Zhu, K. Yvind, J. Dong, M. Galili, H. Hu, N. A. Mortensen, S. Xiao, and L. K. Oxenløwe, "Ultra-compact integrated graphene plasmonic photodetector with bandwidth above 110 GHz," Nanophotonics **9**, 317–325 (2020).
60. L. Zhang, L. Jie, M. Zhang, Y. Wang, Y. Xie, Y. Shi, and D. Dai, "Ultrahigh-Q silicon racetrack resonators," Photon. Res. **8**, 684–689 (2020).
61. T. Hao, Y. Liu, J. Tang, Q. Cen, W. Li, N. Zhu, Y. Dai, J. Capmany, J. Yao, and M. Li, "Recent advances in optoelectronic oscillators," Adv. Photon. **2**, 044001 (2020).
62. L. R. Cortés, D. Onori, H. G. de Chatellus, M. Burla, and J. Azaña, "Towards on-chip photonic-assisted radio-frequency spectral measurement and monitoring," Optica **7**, 434–447 (2020).
63. Z. Tang, S. Pan, and J. Yao, "A high resolution optical vector network analyzer based on a wideband and wavelength-tunable optical single-sideband modulator," Opt. Express **20**, 6555–6560 (2012).
64. T.-Y. Liow, K.-W. Ang, Q. Fang, J.-F. Song, Y.-Z. Xiong, M.-B. Yu, G.-Q. Lo, and D.-L. Kwong, "Silicon modulators and germanium photodetectors on SOI: monolithic integration, compatibility, and performance optimization," IEEE J. Sel. Top. Quantum Electron. **16**, 307–315 (2009).